A multi-purpose imaging endstation for high-resolution micrometer-scaled sub-second tomography

Goran Lovric[a,b,*], Rajmund Mokso[c], Christian M. Schlepütz[a], Marco Stampanoni[a,d]

[a]*Swiss Light Source, Paul Scherrer Institute, 5232 Villigen, Switzerland*
[b]*Centre d'Imagerie BioMédicale, École Polytechnique Fédérale de Lausanne, Lausanne 1015, Switzerland*
[c]*Max IV Laboratory, Lund University, SE-221 00 Lund, Sweden*
[d]*Institute for Biomedical Engineering, ETH Zurich, 8092 Zurich, Switzerland*

Abstract

Time-resolved imaging of dynamic processes, ranging from biological *in vivo* studies to materials under *in situ* and *in operando* conditions, requires a flexible endstation capable of controlling complex components that interact in different configurations and at high speeds. At the X02DA TOMCAT beamline we have recently achieved *in situ* tomographic measurements at a rate of 20 Hz. Independently, we have shown the feasibility of *in vivo* lung imaging down to the micrometer scale. In the present paper, we discuss the latest developments in view of instrumentation and the accompanying components for achieving these two types of measurements. As the prime example, we focus on the technical requirements for *in vivo* tomographic microscopy of the lung at the micrometer scale in terms of acquisition schemes, triggering and radiation dose. We identify ultra-short single-projection exposures combined with accurate triggering capabilities as the main prerequisites to obtain high-quality reconstructions while limiting the X-ray dose imparted on the living sample. The presented endstation offers generic high-speed imaging capabilities, as it is compatible with a variety of experimental setups and suitable for a wide range of time-resolved studies.

Keywords: X-ray imaging, in-vivo, time-resolved tomography
2010 MSC: 92C55, 92C50

1. Introduction

Capturing in three dimensions the time-resolved structural information of fast dynamic processes requires short exposure times, high frame rates and efficient tomographic acquisition protocols. At the tomography beamline [1] of the

---

Swiss Light Source, we advanced high-resolution live animal imaging by correlating the individual frames with the motion of the living sample [2]. These correlative approaches coupled with prospective or retrospective gating perform particularly well in the case of essentially periodic processes such as those found in many biological systems. More recently, *in situ* crack propagation dynamics during tensile tests using synchrotron tomography were reported for the first time with a frequency of 20 tomograms per second [3]. In all cases, advanced triggering and synchronization is indispensable for capturing the dynamics at the desired state, which can either be externally induced, for example, by a compression rig or a high temperature furnace [4], or occur spontaneously and autonomously, as is the case for most *in vivo* samples [5]. Regardless of whether materials science or biological applications are concerned, the efficient integration of the sample controls and monitoring systems (furnace, small animal ventilator, compression rig, etc.) into the beamline infrastructure plays a central role in reducing the X-ray exposure, and hence the radiation dose received by the sample, while resolving the process under investigation in the greatest achievable detail.

Commercially available scanners are capable of routinely performing *in vivo* X-ray computed tomography of small animals down to a spatial resolution of about $10\,\mu$m [6]. At this level of detail, the synchronization of the image acquisition with the biological processes such as the heart beat is solved. New insights into the functional anatomy of various organs may, however, be gained by improving the spatial and temporal resolution further. As a result, the corresponding motion synchronization becomes very challenging. Likewise, in high-resolution X-ray imaging with dose-sensitive samples, the radiation dose is directly linked to the desired spatial resolution, where resolving more and finer details means also a higher X-ray dose. Due to these technical difficulties in pushing the 3D spatial resolution to below about $10\,\mu$m, *in vivo* synchrotron-based lung imaging studies have been restricted until recently to mainly radiographic and particle tracking type experiments [7, 8, 9, 10].

To achieve micrometer-scale resolution tomography at X-ray doses compatible with *in vivo* experiments, we need to be able to interpret the X-ray phase shifting properties of the sample (phase contrast imaging) in addition to the attenuation map used in all conventional medical CTs and small animal μCTs [11]. This implies the use of synchrotron radiation sources for their superior coherence properties and the much higher X-ray flux necessary to achieve sufficiently short exposure times. We have recently detailed this aspect in the case of tomographic lung imaging at the level of alveoli, where we have shown with fresh *ex vivo* mouse samples that micrometer spatial and sub-second temporal resolutions are feasible [12].

In this paper we present a route to implementing micrometer-resolution fast *in vivo* tomographic microscopy of rodent lungs. The main focus lies on the data acquisition, where we describe the technical solutions in view of instrumentation enabling a wide range of synchrotron-based time-resolved studies. These technical aspects are then discussed in light of *in vivo* measurements aimed at gaining a deeper understanding of lung physiology at the microscopic level.

2

2. Experimental methods and instrumentation

2.1. Rotation stage design

Performing micro-tomographic experiments to image processes with ideally (sub-)micrometer resolutions, requires high-precision angular and translational sample positioning, in conjunction with a sample rotation that occurs at rotation speeds that can vary by orders of magnitude, depending on the respective tomographic acquisition setting. Thus, the mechanical errors (radial, axial wobble and tilt) must be kept at a minimum to ensure motion-less and artifact-free CT reconstructions. In particular, the motion errors should be kept below 100 nm at the sample position (about 150 mm above the rotation table) to allow for nanoscopic imaging [13].

Here, we propose a combined semi-custom designed sample-manipulator and rotation axes system. The complete system is depicted in Fig. 1, where both the rotation axes unit and its implementation on the optical table of the X02DA TOMCAT beamline are visible. On top of the rotation axes, two linear trans-
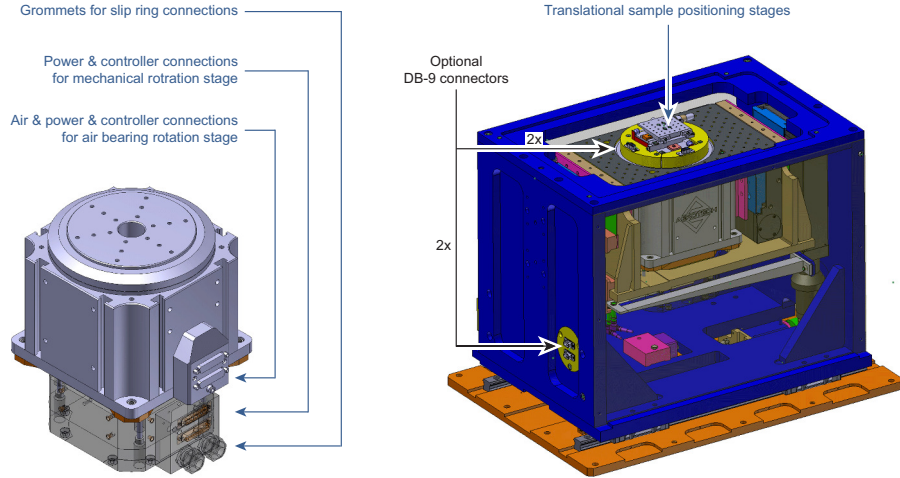

Figure 1: CAD drawings of the rotation axes system and its integration at the endstation. The system (left scheme) consists of a high-precision air bearing rotation stage that is synchronized with a mechanical rotation stage underneath, which drives the slip ring with its 60 cable connections. The grommets of these connections are clearly visible in the bottom part. The whole system is integrated in a custom-made sample manipulator stage (right scheme), and two additional stages are mounted on top for region-of-interest selection when performing CT-scans.

lation stages are used for aligning the desired region-of-interest (ROI) when conducting tomography. For powering these stages (both the encoders as well as the electrical stepper motors), a slip-ring with 60 lead-throughs is used which further enables the transfer of digital and analog signals from the rotating top of the rotation stage to the fixed part below the axis. Two additional vacant D-Sub/DB-9 connectors are available for arbitrary user-specific connections. For

decoupling the high-precision angular movement from any mechanical parts and vibrations, the complete rotation axes unit is implemented as a combined air bearing rotation axis (ABRT-200, Aerotech Inc.) synchronized with a mechanical rotation stage (ADRS-150, Aerotech Inc.) to drive the slip ring. This design assures that the high-precision positioning accuracy of the air bearing stage is not affected by the drag of the slip-ring during rotation. Additional mechanical locks are installed between the two rotation stages to prevent potential cables twisting in case the two stages lose their synchronization (e. g. if one fails).

From the controls point of view, the axes pair is operated in a master-slave mode and interacts with the Aerotech software running on a dedicated PC with a real-time extension. The in-house developed control software interfaces to the hardware via an EPICS driver implementation [14], by which the rotation stage can be powered in different flexible modes to synchronize with the detector and/ or other external devices by use of standard transistor-transistor logic (TTL) triggering. These triggering modes are implemented through so-called "tasks" in the Aerobasic programming language (representing an integrative part of the Aerotech A3200 software controller) and are mainly based upon Aerotech's position-synchronized output (PSO) system, of which the following are currently available:

1. **Fixed distance trigger**: The user first specifies an arbitrary angular distance (e. g. 180°) and width of a pulse (e. g. 10 ms). When the stage starts rotating, it fires trigger signals (voltages) toggling between "HIGH" (+5 V) and "LOW" (0 V), each time it has rotated through the angular distance. Additionally, an offset for the starting point can be set, as well as the total number of trigger signals to be sent.

2. **Snap and step**: An external trigger signal initiates a move by a user-defined rotation angle. The stage sends back a trigger signal once it has completed the requested move, and then waits for the next input trigger to start the subsequent move. Used in conjunction with a camera's "exposure" trigger (from the rotation stage output) and the cameras "busy" signal (with its trailing edge triggering the next angular motion), one obtains perfect synchronization between the data acquisition and sample rotation processes. This mode is used for high-precision "slow" tomography.

3. **Sequence mode**: This is the most flexible mode, where several trigger sequences can be defined. Each sequence defines a number of repetitions and two angular ranges: the TTL signal is set to "LOW" for the first and to "HIGH" for the second range. Multiple such sequences can be executed sequentially. This is best illustrated through an example: Setting both the "LOW" and "HIGH" ranges to 180°, the rotation axis will output a continuous "LOW" TTL signal for the first 180 degrees followed by a "HIGH" signal for the next 180 degrees, repeating this same pattern for subsequent 360° turns. This way, one can obtain a specified number of tomographic scans with identical orientations during the continuous rotation of the sample. This is particularly useful in various time-resolved studies and can be modified to match the exact needs of the experiment.

4

In addition to these modes, the velocity and acceleration (in both negative and positive rotation direction) can be arbitrarily set/changed for each measurement as well as different offsets can be defined.

2.2. Sample alignment

Sample alignment is performed using two linear translation stages on top of the rotation axis that are used for both centering the sample on the axis as well as defining the field of view (FOV) in (local) region-of-interest tomography. For this purpose, we have developed a so-called "off-beam sample alignment" procedure where the sample and the respective region of interest (ROI) is aligned prior to exposing the sample with X-rays. An additional alignment camera is placed perpendicular to the X-ray beam and interfaces to the beamline controls system via the "areaDetector" EPICS application [15]. The detailed scheme is shown in Fig. 2 and can be explained as follows. Using an alignment pin
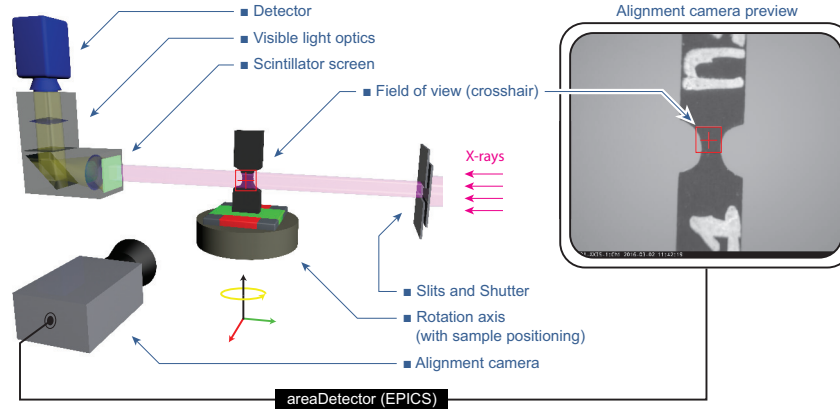

Figure 2: Off-beam sample alignment procedure. The crosshair and box on the live alignment camera preview are calibrated to match the X-ray beam center and size at the sample position.

in the X-ray beam, the ROI (red square in Fig. 2) on the alignment camera is adjusted in size and position to match the field of view of the X-ray detector. The centering and ROI selection on the real samples is then performed without exposure to X-rays by monitoring their position purely with the live preview video. Subsequently, the X-ray tomographic acquisition is launched. The achieved positioning precision is in the order of tens of micrometers and the whole procedure is particularly useful in dose-sensitive experiments where the sample is only exposed to X-rays during image acquisition.

2.3. Flux measurement and dosimetry

A further need in dose sensitive imaging experiments, besides the precise sample pre-alignment, is the accurate determination of the administered X-ray dose itself, especially when aiming towards photon-efficient imaging techniques.

5

While the assessment of radiation dose represents a standardized procedure, it is all the more important in synchrotron-based microscopy techniques where the X-ray fluence is typically orders of magnitudes higher than in standard (X-ray tube) setups. Although various devices are routinely employed at synchrotrons, such as thermoluminescent dosimeters (TLD-s), metaloxidesemiconductor field-effect transistors (MOSFET-s), positive intrinsic negative (PIN) diodes and parallel-plate ionization chambers [16, 17, 18], usually an accurate calibration is necessary to conduct absolute flux measurements.

Here, we present a cost-efficient system consisting of high-precision passivated implanted planar silicon (PIPS) diode coupled to a multi-gain low-current amplifier that was subsequently calibrated by cryogenic radiometry, achieving precisions with less than 2% uncertainty [19, 20]. The complete system is shown in Fig. 3 and consists of a $500\,\mu$m PIPS diode (CANBERRA Industries Inc.) with a custom-made casing (designed by B. Meyer and C. Frieh, LSK/SYN-group of PSI), a multi-gain low-current amplifier (FEMTO Messtechnik GmbH) and remote gain controls implemented in EPICS. The inner workings
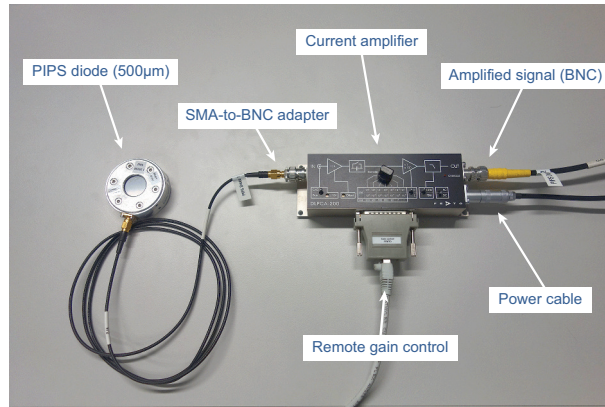

Figure 3: Absolute flux measurement system consisting of a PIPS diode and a multi-gain current amplifier. Both the SMA (SubMiniature version A) and BNC (Bayonet Neill-Concelman) represent standard coaxial radio frequency connectors.

are shown in Fig. 4. To reduce the dark noise, the PIPS chip is covered with a $25\,\mu$m Kapton CB foil which is an opaque, black substrate film offering low light transmission, reflectivity and superior durability. The diodes can also be used in white-beam configuration as they permit high temperature loads up to 100 °C.

2.4. Trigger signaling

Another central challenge for fast tomographic measurements is the synchronization and triggering of all of the involved devices and measurements. Typically, one device or process will drive the entire data acquisition chain, and the necessary synchronization signals will have to be distributed to the remaining components.
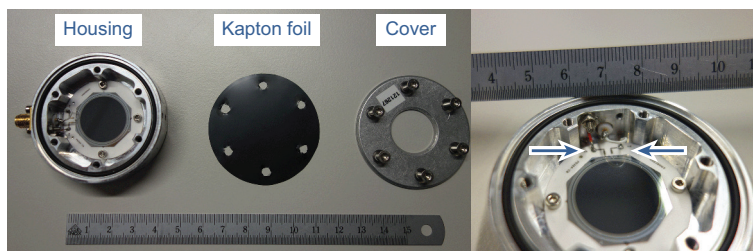
Figure 4: Inner workings of the PIPS diode. The PIPS chip is covered with a $25\,\mu$m dark kapton foil that is sealed with a (dark) rubber band to prevent visible light increasing the dark current of the detector. The arrows in the right part of the image indicate the connectors from the PIPS chip.

To this end, a number of signal processing and recording devices have been integrated into the EPICS beamline control system, either through custom-made drivers or as already supported devices in the synApps distribution [21]:

- **Signal distribution box**: A small FPGA-based device that is capable of routing logical signals (TTL) between a number of input and output connections in all possible directions. An upgrade of the device support is in progress and will allow for output signals to be time delayed with respect to the connected input.

- **Signal generator**: The signal generator can produce custom-defined sequences of output pulses (TTL) with configurable pulse width, period and repetitions.

- **Digital signal acquisition (DAQ) module**: The USB-1608GX-2AO multifunction signal acquisition module from Measurement Computing for analog input/output operations with EPICS support (through the synApps "measComp" module) is capable of sampling analog voltage input signals with up to 500 kHz sampling rates. The acquisition can be triggered via a TTL input signal. Other features include synchronized analog waveform generator output signals, pulse counters, and a pulse generator.

- **Multichannel scaler**: Device to count TTL pulses from multiple sources. On-board memory allows the acquisition of time-series, where the channel advance to the next array element can be triggered externally (for example, using the exposure trigger from a camera). The counting can also be gated with an external signal. Scalers are typically used to time-integrate signals. For instance, it is standard practice to measure the integrated incident x-ray flux during an exposure by passing an ionization chamber voltage signal through a voltage to frequency converter.

As one example of a typical use case, let us consider an experiment where the response of a material inside a tension rig is to be measured for various

7

stages during the tensioning cycle. The user wants to acquire one tomographic dataset before a tensioning step, and a few more immediately following the step to observe the time-dependent response. To assure the same orientation of the reconstructed datasets, we use the sequence mode of the Aerotech rotation stage (described earlier) to trigger a new 180 degree data acquisition with the specified number of frames exactly when the rotation stage passes a given angular position during each revolution of a continuous rotation. The entire measurement is initiated by the user starting the scan. The rotation stage first accelerates to the nominal rotation speed and then sends the first rising edge of the enable signal as it passes through the reference position. This enable signal is directly passed to the fast shutter, which opens with a latency of approximately 20 milliseconds. Passing through a delay generator with a 30 millisecond delay, the enable signal is then sent to the fast camera, which will immediately start acquiring frames. Additionally, the same signal might be passed to the DAQ module that could monitor the voltage response of an external strain gauge with a given sampling frequency. Using the camera's exposure output signal as a trigger, we record the incident beam intensity measured by the PIPS diodes after voltage to frequency conversion in the multichannel scaler and simultaneously trigger the readout of the Aerotech encoder position into an array of measured angular readback positions. Thus, we obtain exactly time-synchronized auxiliary measurements for each camera frame. Finally, after acquiring the specified number of frames, the camera's busy output signal returns to low, which should trigger the closing of the fast shutter and initiate the tension step of the rig on the first cycle. This same sequence is repeated a number of times for each complete revolution of the rotation axis.

The above example illustrates how (a) complex signaling and triggering schemes are necessary to make full use of the ultra-fast acquisition capabilities, and (b) that the details of the acquisition chain can vary substantially from experiment to experiment. It is therefore paramount to provide a flexible infrastructure that can be easily adapted to the particular needs of a given measurement and that offers all of the required functionality within a single controls framework (EPICS).

2.5. Image acquisition and PIV analysis

For acquiring the images we utilized our previously reported experimenal setup [12]. The X-ray beam was monochromated with a double-multilayer monochromator and tuned to 21 keV, which yielded a sufficiently good trade-off between phase contrast and available X-ray flux. The sample was placed at a distance of 25 m to the X-ray source (2.9 T superbend, 2.4 GeV storage ring, ring current $I = 400$ mA, top-up mode) [1]. We used a high-speed CMOS detector (pco.Dimax) coupled to visible-light optics with a 20 μm and 100 μm-thick scintillator for high and medium spatial resolutions, respectively. The two visible-light optics produced effective pixel sizes of $1.1 \times 1.1 \, \mu\text{m}^2$ and $2.9 \times 2.9 \, \mu\text{m}^2$. The first is achieved by using a standard $10\times$ magnifying microscopy objective while the latter is a custom-made (Elya Solutions s.r.o.) high numerical aperture (NA) system with continuously changeable magnification in the range of

8

$2 - 4\times$. The system has been designed for best light throughput and features a NA = 0.17 for the $2\times$ magnification and NA = 0.22 for the $4\times$ magnification.

The measurements were performed *in vivo* and *ex vivo* on adult mice (n = 2 / Balb-C, central animal facility of the University of Bern). Each animal was anesthetized with an injection of a mixture of Fentanyl (0.05 mg), Midazolam (5.0 mg) and Medetomidine (0.5 mg), where the dosages are given per kg body weight. Subsequently, a tracheotomy was performed, the animal was placed into a custom-made sample-holder and the endotracheal canula was mounted and fixed. The animal was then transferred to the beamline hutch, mounted on the sample manipulator (rotation axis) and externally ventilated with a small animal ventilator (FlexiVent, SCIREQ Inc.). After aligning the FOV to a central region of the lung, images were acquired by inducing a short breath-hold phase in the animal's lung with a pressure of $10\,\mathrm{cmH_2O}$ and by continuous exposures with $13\,\mathrm{ms}$ single-exposure times and total duration of approximately 6 seconds. After this procedure was completed, the animal was administered an overdose of pentobarbital (typically in the order of $5\,\mathrm{mg}$ per kg body weight), after which ultra-fast tomograms of the lung were acquired, following our established acquisition and reconstruction protocol [12]. All parts of the animal experiments were approved and supervised by the Swiss Agency for the Environment, Forest and Landscape, and the Veterinary Service of the Canton of Bern.

To examine heart-induced motions at high-resolution, so-called displacement maps were calculated from the dynamic radiographic images by means of the normalized cross-correlation method, where patches of the images from different time points are matched with each other. The complete approach represents a so-called "template matching" problem and is schematically sketched in Fig. 5. First, pairs of two images (with 1008×1008 pixels) are extracted from the time
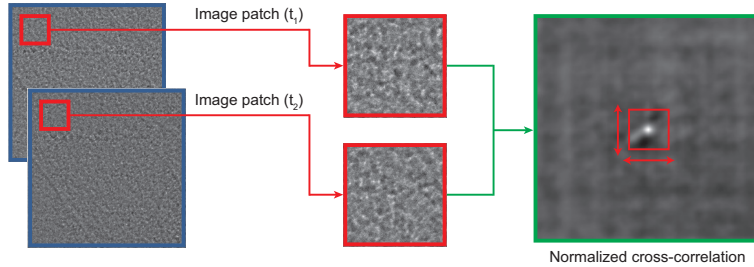

Figure 5: Demonstration of the template matching problem. Two images from the time series $(t_1, t_2, t_3, \ldots)$ are taken, from which individual patches are extracted. For each pair of image patches, the normalized cross-correlation is calculated. The peak position of the latter one yields the displacement in x and y direction of the two images in respect to each other.

series and divided into about 144 interrogation windows (patches) per image pair with sizes of 256×256 pixels. Each pair of image patches is then passed to a template-matching algorithm to calculate the spatial displacement as a function of time [22]. This is repeated for all images from the time series.

9

Additionally, the results were cross-checked with an established time-resolved particle image velocimetry (PIV) system [23], which offers long-time recording capability with the possibility to obtain velocimetry fields with sub-pixel resolutions, however, at the cost of increased computation time. Since PIV involves the statistical analysis of displacements between consecutive pairs of images of tracer particles taken at different time points, it is fully equivalent to the aforementioned template matching problem [24].

3. Results and discussion

3.1. Absolute flux measurements

Using the aforementioned PIPS diode, the X-ray flux is obtained by:

$$F\,[\text{photons/s/mm}^2] = C_{\text{calib}}(E) \cdot \frac{I\,[\text{A}]}{E\,[\text{eV}] \cdot A\,[\text{mm}^2]}, \tag{1}$$

where C_{calib} are the energy-dependent calibration values, I is the measured current in the diode (being typically on the order of $10^{-3} - 10^{-6}$ A), E is the monochromatic X-ray energy and A is the area of the field-of-view (defined with the vertical and horizontal slits, as displayed in Fig. 2).

Despite the ultra-precise diode calibration uncertainty (which is typically less than 1%, but can amount up to a few percent with X-ray energies higher than 40 keV), we identified several measurement uncertainties and reading errors that contribute to the overall physical uncertainty of the X-ray flux determination system. Starting with the diode current, we found an approximate reading error ΔI of $1 - 3\%$ affiliated with the current noise as well as originating from a possible diode misalignment in the beam (i.e. if the diode is slightly titled, resulting in a bigger interaction volume of the X-ray photons and thus in a slightly increased diode current). Another calculation uncertainty originates from the fact that the X-ray energy exhibits a bandwidth uncertainty which we have earlier quantified for the case of the multilayer monochromator with $\Delta E \leq 0.2$ keV [25]. Finally, the area A of the field-of-view exhibits a reading error ΔA which we assume to be in the order of a few pixels corresponding to the detector's resolution limit, e.g. 4 pixels reading error over a lateral/vertical field-of-view size of about 1000 pixels.

For the total uncertainty analysis, we estimated the maximum error margin numerically by estimating single uncertainty sources:

$$\Delta F = \max \left| (C \pm \Delta C) \cdot \frac{I \pm \Delta I}{(E \pm \Delta E) \cdot (A \pm \Delta A)} \right|. \tag{2}$$

The results from the flux measurements and the uncertainty analysis are summarized in Tab. 1. The energy-dependent values result from both the bending magnet spectrum as well as the fact that standardly various filter compositions are used for each energy. For the first flux value at 21 keV, we determined a physical uncertainty of $\Delta F = 0.3 \times 10^{11} \leq 5\%$ of F. For the other values we

obtained similar results, which is why we can define an overall maximum error margin of 5% for all following flux values. Obviously, this error margin can be further reduced by improving the setup (alignment, measurement time, etc.) and it represents only a physical uncertainty for absolute flux values. The error margin for relative measurements (for example, when measuring X-ray absorption by two consecutive measurements with and without an absorbing sample) is negligible. Finally, for each flux value the skin entrance dose values [26] are given in the fourth column of Tab. 1 and were calculated according to

$$D \,[\text{Gy}] = 10^3 \cdot N \cdot \left(\frac{\mu_{\text{en}}}{\varrho} \right) h\nu, \tag{3}$$

where N is the total number of incident photons per cm^2-area, μ_{en}/ϱ is the mass energy absorption coefficient given in cm^2/g and obtained from the NIST database [27] and $h\nu$ is the energy of a single photon given in J. The additional multiplication with 10^3 is necessary to directly translate to entrance dose values given in Gray [Gy].

Table 1: Typical values of the photon flux at the X02DA TOMCAT beamline.

X-ray energy [keV]	Multilayer	Flux [photons/s/mm^2]	Entrance dose (water) [Gy/s]
21	$[\text{Ru/C}]_{100}$	$(7.3 \pm 0.3) \times 10^{11}$	$116 \pm 5\%$
25	$[\text{W/Si}]_{100}$	$(4.3 \pm 5\%) \times 10^{11}$	$47.3 \pm 5\%$
30	$[\text{W/Si}]_{100}$	$(2.1 \pm 5\%) \times 10^{11}$	$15.7 \pm 5\%$
40	$[\text{W/Si}]_{100}$	$(1.4 \pm 5\%) \times 10^{11}$	$6.2 \pm 5\%$
45	$[\text{W/Si}]_{100}$	$(4.1 \pm 5\%) \times 10^{9}$	$0.16 \pm 5\%$

3.2. Heart-induced lung movement

When inducing the constant-pressure breath-holds in the live animals, we observed very fine pressure oscillations in the animal's lungs which occurred at approximately 200 beats per minute (BPM). This is shown in Fig. 6, where a pressure range of $10.2 - 10.4\,\text{cmH}_2\text{O}$ is depicted over an approximate time period of 10 seconds. These pressure oscillations where directly measured in the small animal's ventilator with the so-called airway opening pressure transducer, which gives a secondary feedback when inducing a pressure (curve) into the animals lung. We hypothesized that these pressure changes originate from the movement of the heart inside the animal's thorax, but it was unclear to what degree the pressure oscillations influence the imaging process in high-resolution lung imaging.

To address this question, we acquired a series of projection images with single-exposure times of $13\,\text{ms}$ (with the $1.1\,\mu\text{m}$-pixel-size optics) and over a total scan time of approximately 6 seconds. From these we calculated so-called PIV/displacement maps in dependency on the time. The results are shown in Fig. 7 at different time points between $0\,\text{ms}$ and $208\,\text{ms}$. As can be seen,
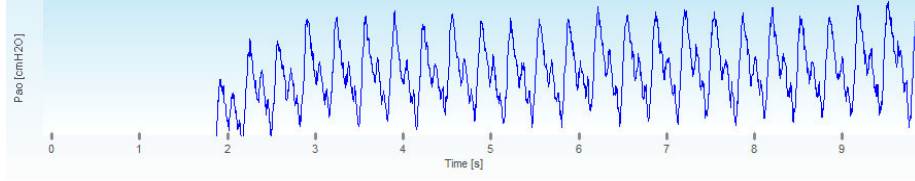
11

Figure 6: Pressure oscillations measured with the FlexiVent small animal ventilator. The vertical scales ranges from 10.2 to $10.4\,\mathrm{cmH_2O}$.
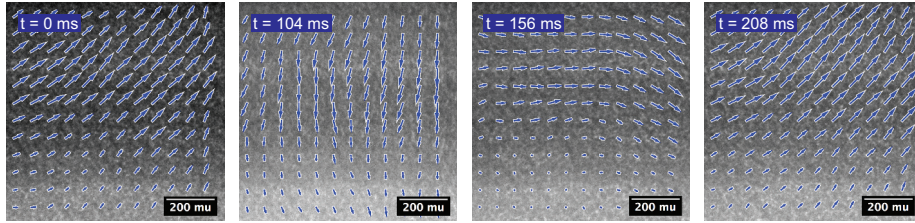

Figure 7: PIV displacement maps at different time points of the heartbeat phase

the displacements are uniformly distributed over the inspected field-of-view, indicating a mostly linear and periodic movement with very small irregularities.

Following this result, the corresponding pixel displacement curves were calculated by averaging over all interrogation windows from the PIV/template matching analysis. These are shown in Fig. 8, where both the temporal vectorial pixel displacements in x- and y-directions (Δx and Δy) as well as the temporal absolute displacement amplitudes ($\sqrt{\Delta x^2 + \Delta y^2}$) are shown. The
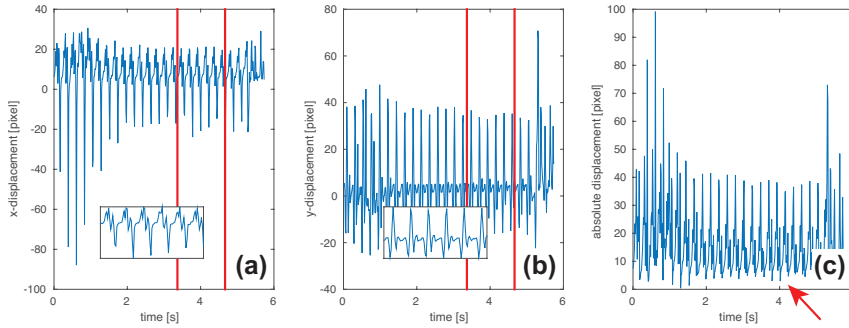

Figure 8: Average pixel displacement curves for all interrogation windows: **(a)** shows the pixel displacement in x-direction; **(b)** in y-direction; and **(c)** shows the absolute displacement amplitude over time. The red arrow indicates the minimum displacement amplitude.

displacements directly correlate to the aforementioned pressure oscillations (see Fig. 6), e.g. the y-direction displacement [Fig. 8 (b)] yielded almost complete qualitative correspondence. We hypothesize that the larger displacements at the beginning and end of the tracing [Fig. 8 (c)] are attributed to the phenomenon

12

of heart rate variability (HRV), stating that single heartbeats undergo a certain variation in time and hence cause also variations in the displacement amplitudes.

From these results we found that the maximum average displacement amplitude is approximately 50 pixels, although the result is superimposed by single outliers. The minimal displacement amplitudes [indicated by a red arrow in Fig. 8 (c)] were found to be in the range of 5-10 pixels, which considering the respective optics amounts to a displacement of $5.5 - 11\,\mu$m over a time period of $13\,$ms (corresponding to the respective single-projection exposure time). Thus, if aiming at resolutions of $1 - 4\,\mu$m, the exposure times have to be reduced by at least a factor of 5, meaning that in such a case single-projection exposure times of less than $3\,$ms will be necessary. In addition to this, the time point of imaging will be crucial since the minimal absolute displacement of a few pixels occurs only during a very short time range, while outside of this time range the absolute displacements are much larger. Thus, we can conclude that the main requirement for *in vivo* tomography at the micrometer scale will necessitate short exposure times in the order of less than a few milliseconds combined with an accurate triggering protocol with direct feedback from the animal's heart beat cycle, for example by using a heart-rate monitor.

3.3. Fast tomography

The next step was to re-evaluate our previously proposed ultra-fast acquisition protocol. Namely, we had concluded earlier that acquisition times of approximately $0.5\,$s per tomogram will be necessary for conducting lung tomography at the micrometer scale, however the data was extrapolated from scans taken at much slower rates [12]. Therefore, in the following we acquired ultra-fast tomograms with freshly sacrificed (intact) animals subsequent to the *in vivo* radiography measurements in order to evaluate general limits towards even faster acquisition schemes.

Images of lung tomographic slices taken with different exposure times and rotation speeds are shown in Fig. 9 and summarized in Tab. 2, where the single-projection exposure times t_{exp} and the single-projection skin entrance doses D_{skin} as well as the total numbers of projections n_{proj}, the total scan times T_{scan} and the so-called total frame times T_{frame} are given. The difference
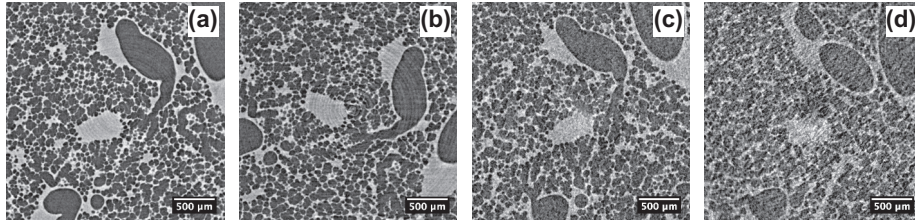

Figure 9: Ultra-fast tomographic slices of mouse lungs (post mortem), located approximately in equivalent lung regions, at different total scan times. The scan parameters for images **(a)**-**(d)** are summarized in Tab. 2.

13

Table 2: Ultra-fast tomographic measurements of mouse lungs. For each scan, the single-projection exposure t_{exp}, the single-projection entrance dose D_{skin} and the total number of projections n_{proj} are given. The total scan time T_{scan} gives the necessary theoretical X-ray exposure time for obtaining the full tomographic scan, while the total frame time T_{frame} additionally accounts for the detector's readout time, which sets an upper limit on the rotation speed.

Scan	t_{exp} [ms]	D_{skin} (water) [mGy/t_{exp}]	n_{proj}	T_{scan} [s]	T_{frame} [s]	v_{rot} [°/s]
(a)	1.25	145	901	1.13	1.16	154
(b)	0.70	81	901	0.63	0.67	270
(c)	0.25	29	901	0.23	0.24	769
(d)	0.25	29	361	0.09	0.09	1903

between the total scan time T_{scan} and the total frame time T_{frame} is that the latter one also accounts for the detector's readout time and ultimately limits the maximum rotation speed v_{rot}. This is illustrated by the fact that both Figs. 9(c) and 9(d) were acquired with reduced field-of-views (1487×615 and $1583 \times 415 \mathrm{\ pixel}^2$, respectively) in order to improve the detector's readout time. A full frame image ($2016 \times 2016 \mathrm{\ pixel}^2$) would lead to increased total frame times that are a few factors higher than the ones given in Tab. 2. Thus, despite the need of reducing the exposure times in order to "catch" fast micrometer-sized heart-induced movements in the lung, the approach cannot be continued arbitrarily.

As can be seen from Fig. 9, the image quality degrades with shorter exposure times, but even with faster rotations we did not observe artifacts that could be affiliated with the rotation speed. Thus, even with total scan times of 0.25 s we were still able to produce tomographic reconstructions with valuable biological features. In view of *in vivo* tomography and by taking into account both the entrance dose values of each scan (3rd column in Tab. 2) as well as the fact that we are dealing with region-of-interest (local) tomography, we can identify different criteria for an optimal tomographic setting: on the one hand, the decrease of T_{scan} is favorable as it directly corresponds to a reduction of radiation dose; on the other hand, this decrease is either achieved by reducing the number of projections or by reducing the single-projection exposure times. While a low-n_{proj}/high-t_{exp} setting will introduce additional artifacts to the image, the inverse setting (high-n_{proj}/low-t_{exp}) represents currently a limiting point arising from the increasing detector's readout time that becomes more pronounced with shorter exposures.

In summary, we can conclude that from a technical point of view fast tomographic acquisitions do not impose limitations to the obtained image quality. Moreover, when reducing single-projection exposure times, the skin entrance dose can be reduced so that the maximal received dose is centered only in the image's field of view, which goes well along with the famous dose-fractionation theorem [28]. However, the process of low-n_{proj}/high-t_{exp} vs. high-n_{proj}/low-

14

t_{exp} remains a competing one which eventually has to be adapted to the respective sample.

4. Conclusions

We have presented a beamline endstation design suitable for time-resolved synchrotron-based tomographic studies at the micrometer scale, from biological experiments to various studies in materials science. By utilizing a low-cost absolute flux measurement device we measured typical entrance doses in the order of $20 - 100\,\mathrm{Gy}$ per second. Although such high X-ray fluxes are necessary to enable high-speed tomography, they also lead to the fact that a sophisticated sample alignment technique becomes necessary, for which we have demonstrated a off-beam sample alignment setup that does not require the use of X-rays. The implementation with a fast high-precision rotation axes system coupled to a trigger signaling scheme was presented to enable a wide range of triggering and synchronization schemes.

As a first example we evaluated the requirements for *in vivo* tomographic imaging of the lung at the micrometer scale. We conclude that exposure times of less than $3\,\mathrm{ms}$ are necessary, combined with accurate triggering in order to avoid any artifacts coming from the heart movement. We showed that exposure times can be shortened down to the sub-millisecond regime, but the detector's readout time imposes a clear limitation to this process. This affects in particular region-of-interest tomography, where the imaging with a low-exposure-time and high-number-of-projection setting is favored in terms of image quality.

Acknowledgments

References

[1] M. Stampanoni, A. Groso, A. Isenegger, G. Mikuljan, Q. Chen, A. Bertrand, S. Henein, R. Betemps, U. Frommherz, P. Böhler, D. Meister, M. Lange, R. Abela, Trends in synchrotron-based tomographic imaging: the SLS experience,

in: Proceedings of SPIE, Vol. 6318, SPIE, 2006, pp. 63180M–1–14.
`doi:10.1117/12.679497`.
URL `http://link.aip.org/link/PSISDG/v6318/i1/p63180M/s1{&}Agg=doi`

[2] R. Mokso, D. A. Schwyn, S. M. Walker, M. Doube, M. Wicklein, T. Müller, M. Stampanoni, G. K. Taylor, H. G. Krapp, Four-dimensional in vivo X-ray microscopy with projection-guided gating, Scientific Reports 5 (2015) 8727. `doi:10.1038/srep08727`.
URL `http://www.nature.com/doifinder/10.1038/srep08727http://www.nature.com/articles/sre`

[3] E. Maire, C. Le Bourlot, J. Adrien, A. Mortensen, R. Mokso, 20 Hz X-ray tomography during an in situ tensile test, International Journal of Fracture`doi:10.1007/s10704-016-0077-y`.
URL `http://link.springer.com/10.1007/s10704-016-0077-y`

[4] J. L. Fife, M. Rappaz, M. Pistone, T. Celcer, G. Mikuljan, M. Stampanoni, Development of a laser-based heating system for in situ synchrotron-based X-ray tomographic microscopy, Journal of Synchrotron Radiation 19 (3) (2012) 352–358. `doi:10.1107/S0909049512003287`.

[5] J. Moosmann, A. Ershov, V. Altapova, T. Baumbach, M. S. Prasad, C. LaBonne, X. Xiao, J. Kashef, R. Hofmann, X-ray phase-contrast in vivo microtomography probes new aspects of Xenopus gastrulation, Nature 497 (7449) (2013) 374–377. `doi:10.1038/nature12116`.
URL `http://www.nature.com/doifinder/10.1038/nature12116`

[6] D. Clark, C. Badea, Micro-ct of rodents: State-of-the-art and future perspectives, Physica Medica 30 (6) (2014) 619 – 634. `doi:http://dx.doi.org/10.1016/j.ejmp.2014.05.011`.
URL `http://www.sciencedirect.com/science/article/pii/S1120179714001008`

[7] A. Fouras, B. J. Allison, M. J. Kitchen, S. Dubsky, J. Nguyen, K. Hourigan, K. K. W. Siu, R. A. Lewis, M. J. Wallace, S. B. Hooper, Altered lung motion is a sensitive indicator of regional lung disease., Annals of Biomedical Engineering 40 (5) (2012) 1160–9. `doi:10.1007/s10439-011-0493-0`.
URL `http://www.ncbi.nlm.nih.gov/pubmed/22189492`

[8] S. Dubsky, S. B. Hooper, K. K. W. Siu, A. Fouras, Synchrotron-based dynamic computed tomography of tissue motion for regional lung function measureme Journal of the Royal Society, Interface 9 (74) (2012) 2213–2224. `doi:10.1098/rsif.2012.0116`.
URL `http://www.ncbi.nlm.nih.gov/pubmed/22491972`

[9] R. P. Murrie, K. S. Morgan, A. Maksimenko, A. Fouras, D. M. Paganin, C. Hall, K. K. W. Siu, D. W. Parsons, M. Donnelley, Live small-animal X-ray lung velocimetry and lung micro-tomography at the Australian Synchrotron Ima Journal of Synchrotron Radiation 22 (4) (2015) 1049–1055.

16

doi:10.1107/S1600577515006001.
URL http://scripts.iucr.org/cgi-bin/paper?S1600577515006001

[10] R. P. Murrie, D. M. Paganin, A. Fouras, K. S. Morgan,
Phase contrast x-ray velocimetry of small animal lungs: optimising imaging rates,
Biomedical Optics Express 7 (1) (2016) 79. doi:10.1364/BOE.7.000079.
URL https://www.osapublishing.org/abstract.cfm?URI=boe-7-1-79

[11] R. Mokso, F. Marone, S. Irvine, M. Nyvlt, D. Schwyn, K. Mader,
G. K. Taylor, H. G. Krapp, M. Skeren, M. Stampanoni,
Advantages of phase retrieval for fast x-ray tomographic microscopy,
Journal of Physics D: Applied Physics 46 (49) (2013) 494004.
doi:10.1088/0022-3727/46/49/494004.
URL http://stacks.iop.org/0022-3727/46/i=49/a=494004?key=crossref.b6573dce28ec3bc116017

[12] G. Lovric, S. F. Barré, J. C. Schittny,
M. Roth-Kleiner, M. Stampanoni, R. Mokso,
Dose optimization approach to fast X-ray microtomography of the lung alveoli,
Journal of Applied Crystallography 46 (4) (2013) 856–860.
doi:10.1107/S0021889813005591.
URL http://scripts.iucr.org/cgi-bin/paper?S0021889813005591http://doi.org/n3p

[13] M. Stampanoni, R. Mokso, F. Marone, J. Vila-Comamala, S. Gore-
lick, P. Trtik, K. Jefimovs, C. David, Phase-contrast tomography at the
nanoscale using hard x rays, Physical Review B 81 (14) (2010) 1–4.
doi:10.1103/PhysRevB.81.140105.

[14] EPICS group, Experimental physics and industrial control system,
http://www.aps.anl.gov/epics/ (2015).

[15] Mark Rivers, areaDetector: EPICS software for area detectors,
https://github.com/areaDetector (2015).

[16] T. Kron, L. Duggan, T. Smith, A. Rosenfeld,
M. Butson, G. Kaplan, S. Howlett, K. Hyodo,
Dose response of various radiation detectors to synchrotron radiation.,
Physics in Medicine and Biology 43 (11) (1998) 3235–59.
URL http://www.ncbi.nlm.nih.gov/pubmed/9832014

[17] N. Nariyama, Ion recombination in parallel-plate free-air ionization chambers for synchrotron radiation.,
Physics in Medicine and Biology 51 (20) (2006) 5199–209.
doi:10.1088/0031-9155/51/20/008.
URL http://www.ncbi.nlm.nih.gov/pubmed/17019033

[18] A. K. Bakshi, S. Chatterjee, T. Palani Selvam, B. S. Dhabekar,
Study on the response of thermoluminescent dosemeters to synchrotron radiation: experimental method
Radiation Protection Dosimetry 140 (2) (2010) 137–46.
doi:10.1093/rpd/ncq107.
URL http://www.ncbi.nlm.nih.gov/pubmed/20308052

17

[19] M. Krumrey, M. Gerlach, M. Hoffmann, P. Muller, Thin Transmission Photodiodes as Monitor Detectors in the X-ray Range, AIP Conference Proceedings 879 (1) (2007) 1145–1147. doi:10.1063/1.2436266.
URL http://link.aip.org/link/APCPCS/v879/i1/p1145/s1{&}Agg=doi

[20] M. Gerlach, M. Krumrey, L. Cibik, P. Müller, H. Rabus, G. Ulm, Cryogenic radiometry in the hard x-ray range, Metrologia 45 (5) (2008) 577–585. doi:10.1088/0026-1394/45/5/012.
URL http://stacks.iop.org/0026-1394/45/i=5/a=012?key=crossref.9051965cffc80185276381feb

[21] BCDA Group, Advanced Photon Source, synApps, https://www1.aps.anl.gov/bcda/synapps (2015).

[22] J. P. Lewis, Fast Template Matching, in: Vission Interface, Vol. 95, Canadian Image Processing and Pattern Recognition Society, 1995, pp. 120–123.
URL http://citeseerx.ist.psu.edu/viewdoc/download?doi=10.1.1.157.3888{&}amp;rep=rep1{&}

[23] Z. J. Taylor, R. Gurka, G. A. Kopp, A. Liberzon, Long-Duration Time-Resolved PIV to Study Unsteady Aerodynamics, IEEE Transactions on Instrumentation and Measurement 59 (12) (2010) 3262–3269. doi:10.1109/TIM.2010.2047149.
URL http://ieeexplore.ieee.org/lpdocs/epic03/wrapper.htm?arnumber=5464317

[24] S. C. Irvine, D. M. Paganin, S. Dubsky, R. A. Lewis, A. Fouras, Phase retrieval for improved three-dimensional velocimetry of dynamic x-ray blood speckle, Applied Physics Letters 93 (15) (2008) 153901. doi:10.1063/1.3001592.
URL http://link.aip.org/link/APPLAB/v93/i15/p153901/s1{&}Agg=doi

[25] G. Lovric, P. Oberta, I. Mohacsi, M. Stampanoni, R. Mokso, A robust tool for photon source geometry measurements using the fractional Talbot effect, Optics Express 22 (3) (2014) 2745. doi:10.1364/OE.22.002745.
URL http://www.opticsinfobase.org/abstract.cfm?URI=oe-22-3-2745http://doi.org/q9m

[26] M. R. Howells, A. P. Hitchcock, C. J. Jacobsen, Introduction: Special issue on radiation damage, Journal of Electron Spectroscopy and Related Phenomena 170 (1-3) (2009) 1–3. doi:10.1016/j.elspec.2009.01.004.
URL http://linkinghub.elsevier.com/retrieve/pii/S0368204809000176

[27] J. H. Hubbell, S. M. Seltzer, Tables of X-ray Mass Attenuation Coefficients and Mass Energy-Absorption (1996).
URL http://physics.nist.gov/PhysRefData/XrayMassCoef/cover.html

[28] B. F. McEwen, K. H. Downing, R. M. Glaeser, The relevance of dose-fractionation in tomography of radiation-sensitive specimens, Ultramicroscopy 60 (3) (1995) 357–373. doi:10.1016/0304-3991(95)00082-8.

18